

Dielectric function and band structure of $\text{Sn}_{1-x}\text{Ge}_x$ ($x < 0.06$) alloys on InSb

Cite as: Appl. Phys. Lett. **114**, 062102 (2019); doi: [10.1063/1.5086742](https://doi.org/10.1063/1.5086742)

Submitted: 22 December 2018 · Accepted: 17 January 2019 ·

Published Online: 12 February 2019



View Online



Export Citation



CrossMark

Rigo A. Carrasco,¹ Stefan Zollner,^{1,a)}  Stephanie A. Chastang,² Jinsong Duan,² Gordon J. Grzybowski,² Bruce B. Claflin,³ and Arnold M. Kiefer³

AFFILIATIONS

¹Department of Physics, New Mexico State University, P.O. Box 30001, Las Cruces, New Mexico 88003, USA

²KBRwyle, 2601 Mission Point Blvd., Suite 300, Dayton, Ohio 45431, USA

³Air Force Research Laboratory, Sensors Directorate, Wright-Patterson Air Force Base, Ohio 45433, USA

^{a)}Email: zollner@nmsu.edu. URL: <http://ellipsometry.nmsu.edu>

ABSTRACT

Tin-rich $\text{Sn}_{1-x}\text{Ge}_x$ alloys with Ge contents up to 6% were grown pseudomorphically on InSb (001) substrates by molecular beam epitaxy at room temperature. The alloys show a germanium-like lattice and electronic structure and respond to the biaxial stress within continuum elasticity theory, which influences bands and interband optical transitions. The dielectric function of these alloys was determined from 0.16 to 4.7 eV using Fourier-transform infrared and spectroscopic ellipsometry. The E_1 and $E_1 + \Delta_1$ critical points decrease with the increasing Ge content with a bowing parameter similar to the one established for Ge-rich $\text{Sn}_{1-x}\text{Ge}_x$ alloys. On the other hand, the inverted direct bandgap \bar{E}_0 is nearly independent of the Ge content, which requires a bowing parameter of about 0.8 eV, much lower than what has been established using photoluminescence experiments of Ge-rich relaxed $\text{Sn}_{1-x}\text{Ge}_x$ alloys.

Published under license by AIP Publishing. <https://doi.org/10.1063/1.5086742>

Dilute $\text{Sn}_{1-x}\text{Ge}_x$ alloys ($x \ll 1$) are randomly disordered germanium-like semiconductors with an inverted band structure¹ and a negative energy gap of $\bar{E}_0 = -0.41$ eV because the s -antibonding orbital with Γ_7^- symmetry has a lower energy than the p -bonding Γ_8^+ orbital, see Fig. 1(a). Because of the degeneracy of the Γ_8^+ band, the bandgap of unstrained $\text{Sn}_{1-x}\text{Ge}_x$ alloys (with small x) is exactly zero, protected by the cubic symmetry of the crystal. If grown pseudomorphically strained on a suitable substrate (like InSb), the alloys undergo a topological phase transition from a Dirac semimetal ($x < 1.2\%$) to a topological insulator ($x > 1.2\%$) as the in-plane strain changes from compressive to tensile²⁻⁴ (near $x = 1.2\%$ for growth on InSb), see Fig. 1. At some value of x (probably between 25% and 75%), the direct gap \bar{E}_0 becomes zero and changes its sign,⁵⁻⁸ but such alloys have not yet been studied experimentally since Sn and Ge are barely miscible. Thin films of stable $\text{Sn}_{1-x}\text{Ge}_x$ alloys can be grown epitaxially through non-equilibrium growth methods (e.g., molecular beam epitaxy and chemical vapor deposition), allowing their properties to be explored.

Many quantities of $\text{Sn}_{1-x}\text{Ge}_x$ alloys, such as lattice constants and bandgaps, vary smoothly with the composition and

follow Vegard's Law (linear interpolation) with quadratic corrections⁹

$$E(x) = E_{\text{Ge}}x + E_{\text{Sn}}(1-x) - bx(1-x), \quad (1)$$

where the subscripts indicate the element and b is the bowing parameter. A positive bowing parameter indicates that the quantity E for the alloy is smaller than that given by a linear interpolation. Examples of such quantities and their bowing parameters determined from Ge-rich $\text{Sn}_{1-x}\text{Ge}_x$ alloys ($x > 0.85$) are shown in Table S1. Some quantities, especially the inverse effective mass (Luttinger) parameters, diverge as \bar{E}_0 crosses zero and require a different interpolation scheme as explained in the [supplementary material](#).

The purpose of this manuscript is to describe the dielectric function (determined from spectroscopic ellipsometry) and the band structure of $\text{Sn}_{1-x}\text{Ge}_x$ alloys ($x < 0.06$). Our work follows similar studies for Ge-rich alloys^{10,11} and α -tin,¹² but the dielectric function and critical-point (CP) parameters for Sn-rich $\text{Sn}_{1-x}\text{Ge}_x$ alloys have not yet been reported. It is of particular interest if bowing parameters determined on the Ge-rich side can also be applied to Sn-rich alloys.

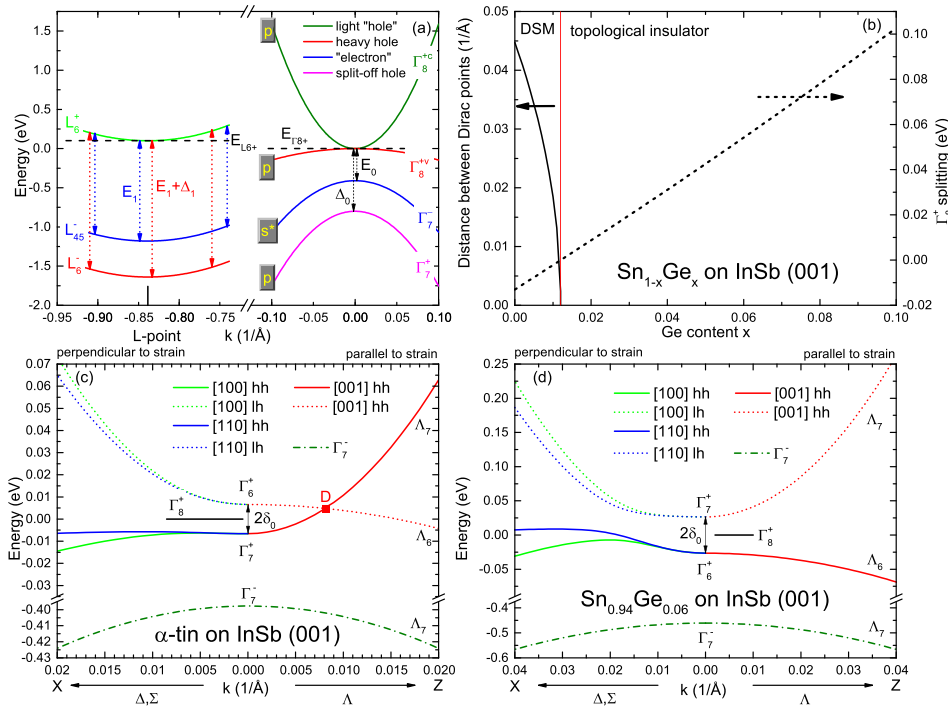


FIG. 1. (a) Schematic of the band structure of unstrained α -tin with interband transitions and band symmetries. (b) Splitting $2\delta_0$ of Γ_8^+ energy levels versus Ge content; separation of the two Dirac points in the Dirac semimetal (DSM) phase. (c) Conduction and valence band energies for wave vectors parallel and perpendicular to the [001] shear strain. Compressive in-plane stress makes α -tin ($x = 0$) a DSM. The Dirac point (D) is indicated. (d) Tensile in-plane stress makes $\text{Sn}_{1-x}\text{Ge}_x$ ($x = 6\%$) on InSb a topological insulator with a small gap.

Our $\text{Sn}_{1-x}\text{Ge}_x$ alloys were grown on InSb (001) substrates by molecular beam epitaxy at room temperature as described previously.^{5,13–15} The composition was varied by changing the Ge effusion cell temperature while keeping the tin flux constant. The growth rate was 8–10 nm/min. Post-growth examination by high-resolution x-ray diffraction (XRD) establishes the diamond crystal structure and high crystalline quality. The Ge content and the layer thickness were determined from the (004) Bragg reflections, assuming that the lattice constant of $\text{Sn}_{1-x}\text{Ge}_x$ varies linearly with the composition¹⁶ (bowing parameter $b = 0$) and that the alloys are fully strained, which was verified with asymmetric XRD reciprocal space maps for selected samples. Pure α -tin on InSb is under compressive in-plane strain, while $\text{Sn}_{1-x}\text{Ge}_x$ alloys on InSb with a Ge content above 1.2% display tensile in-plane strain, see Fig. 2. All the layers reported here were fully strained with strong *Pendellösung* fringes, but thicker alloys at high strain showed some relaxation. Table I describes the layers investigated in this study, especially their composition and thickness.

Ellipsometric angles at room temperature were acquired from 0.16 eV (the bandgap of the InSb substrate) to 4.7 eV at three angles of incidence (65° – 75°) on two different instruments and analyzed as described elsewhere.^{9,15} All pseudo-dielectric function spectra showed E_0 , E_1 , $E_1 + \Delta_1$, and E_2 CPs¹⁷ and one interference fringe between E_0 and E_1 at an energy that depended on the thickness.¹⁵ The data were fitted using a three-layer model (oxide, epilayer, and substrate), and the optical constants of the epilayer were determined using a two-step process. We first described the optical constants of the epilayer using a Kramers-Kronig-consistent semiconductor parametric oscillator model to determine the thicknesses. We then fixed the thicknesses to the values found in the first step, discarded the parametric

oscillator model to avoid bias, and fitted the optical constants of the epilayer independently at each wavelength. Both steps in this fitting process yielded approximately the same optical constants. The overall fit throughout the spectral range was usually better in the parametric oscillator model, while the point-by-point fit gave more accurate results near the CPs and for the calculation of derivative spectra. The point-by-point fit sometimes diverged or produced noise or steps in the data, especially near interference fringes. Such artifacts can be reduced by performing a multi-sample fit for epilayers with different thicknesses (but the same composition) using the same optical constants for all $\text{Sn}_{1-x}\text{Ge}_x$ epilayers (for constant x). Since the optical constants

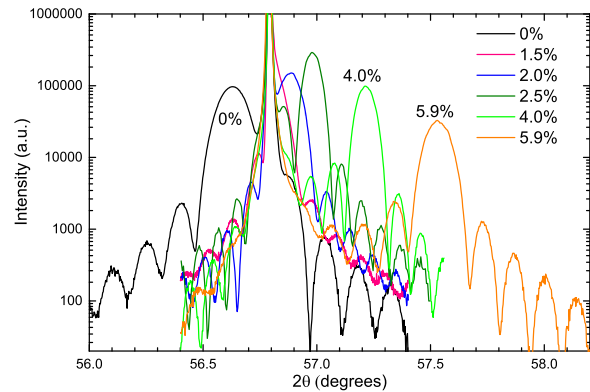


FIG. 2. (004) Bragg reflections of $\text{Sn}_{1-x}\text{Ge}_x$ alloy layers ($x = 0$ – 5.9%) grown on InSb (001) were used to determine the composition and thickness. Alloys below (above) 1.2% Ge are under compressive (tensile) in-plane stress.

TABLE I. Ge content x and thickness t determined from x-ray diffraction (XRD) and spectroscopic ellipsometry (SE). Energies E_i , broadenings Γ_i , and phase angle ϕ of the \bar{E}_0 , E_1 , and $E_1 + \Delta_1$ gaps from SE.

x %	t (XRD) (nm)	t (SE) (nm)	\bar{E}_0 (eV)	E_1 (eV)	$E_1 + \Delta_1$ (eV)	Γ_{E_1} (meV)	$\Gamma_{E_1 + \Delta_1}$ (meV)	ϕ_{E_1} ($^\circ$)
0	67.2	68.6	0.418	1.281	1.739	60	91	74
1.5	97.8	100.4	0.425	1.269	1.719	64	97	70
2.0	100.5	103.4	0.427	1.250	1.707	77	110	73
2.4 ^a		73.9	0.428	1.275	1.738	59	87	98
2.5	119.0	119.7	0.428	1.255	1.709	70	101	64
3.6 ^a	81.4	81.2	0.429	1.245	1.681	54	102	41
4.0	103.4	103.1	0.432	1.263	1.711	67	99	65
4.1 ^a	81.5	81.4	0.428	1.247	1.692	63	101	58
5.0 ^b		188	0.423					
5.6	50.1	50.3	0.433	1.232	1.669	85	129	55
5.9 ^a	75.0	75.1	0.429	1.239	1.665	?	102	40

^aDifficult to fit because of the overlap with an interference fringe.

^bPartially relaxed.

for the native oxide on $\text{Sn}_{1-x}\text{Ge}_x$ alloys are not known, we used the optical constants for the native oxide on InSb instead, similar to our earlier analysis of ellipsometry measurements on α -Sn layers.¹⁵

Figure 3 shows the dielectric function of α -Sn and $\text{Sn}_{1-x}\text{Ge}_x$ alloys from 0.2 to 4.7 eV grown pseudomorphically on InSb (001), as determined from a point-by-point fit. Trends shown by dashed arrows include reduced amplitudes, increased broadenings, a redshift of the E_1 and E_2 CPs, and an increased background at the lowest energies with the increasing Ge content. The \bar{E}_0 peak shows a slight blueshift with increasing x , as shown in the inset.

Two optical interband transitions are easily accessible to spectroscopic ellipsometry to study the band structure of $\text{Sn}_{1-x}\text{Ge}_x$ alloys, see Figs. 1(a) and 3. The \bar{E}_0 gap separates the Γ_7^-

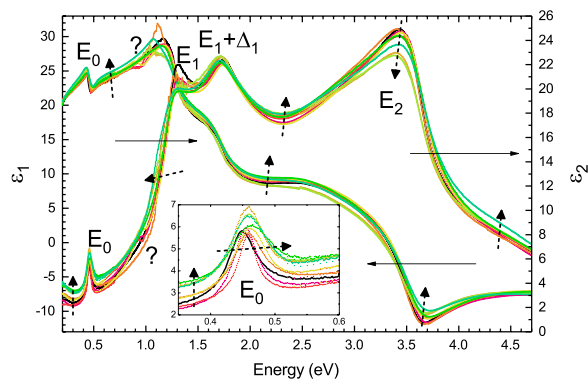


FIG. 3. Dielectric function of α -Sn (black) and $\text{Sn}_{1-x}\text{Ge}_x$ alloys ($x < 0.06$) on InSb (001) from a point-by-point fit to spectroscopic ellipsometry data. Colors from red to blue indicate the increasing Ge content. The magnified inset of ϵ_2 versus photon energy shows a slight blueshift of \bar{E}_0 with the increasing Ge content. The question mark points out a numerical instability of the point-by-point fit near an interference fringe. Dashed arrows show the trends with the increasing Ge content. The tabulated data for this figure are included in the [supplementary material](#).

VB from the Γ_8^+ valence/conduction band. Also, the E_1 and $E_1 + \Delta_1$ transitions occur from the $L_{4,5}^-$ and L_6^- VBs to the L_6^+ CB at the L-point and along the [111] directions.

We first discuss the E_1 and $E_1 + \Delta_1$ CPs since this is more straightforward based on previous research on other materials like Ge.¹⁷ Ellipsometry measurements on Ge, α -Sn, and Ge-rich $\text{Sn}_{1-x}\text{Ge}_x$ alloys established the E_1 and $E_1 + \Delta_1$ energies for the elements and the bowing parameters in the Ge-rich regime, see Table S1. Predictions from previous data, including strain corrections, are shown in Fig. 4 in comparison with our experimental data, which were determined by calculating the second derivatives of the data shown in Fig. 3 and fitting them with two-dimensional CP line shapes of the form^{9,15,17}

$$\epsilon(\hbar\omega) = C - A \ln(\hbar\omega - E_g - i\Gamma)e^{i\phi}, \quad (2)$$

where E_g , A , Γ , and ϕ are the energy, amplitude, broadening, and excitonic phase angle of the CP.

Since the E_1 energies for bulk diamond and zinc blende semiconductors are usually determined with an accuracy of about 1 meV, our experimental data in Fig. 4 show an unexpected amount of scatter, considering that the clearly pronounced XRD peaks in Fig. 2 suggest a high accuracy of the Ge content. Perhaps the presence of an interference fringe just below the E_1 CP affects the accuracy of our second-derivative analysis. Despite these errors, the agreement of our data with the calculated E_1 and $E_1 + \Delta_1$ energies from the established bowing parameters¹⁰ is good. Even better agreement can be achieved, if a single bowing parameter of $b = 1.3$ eV is used to describe the dependence of these CPs on the Ge content, rather than different bowing parameters for E_1 and $E_1 + \Delta_1$.

We now proceed to discuss the dependence of the \bar{E}_0 gap in $\text{Sn}_{1-x}\text{Ge}_x$ alloys on the Ge content. An \bar{E}_0 peak was recently discovered in the dielectric function of α -Sn.¹⁵ Comparing the predictions from the established bowing parameters with experiments is not straightforward because the mechanism giving rise to the \bar{E}_0 peak in ellipsometry data is not fully understood yet. Therefore, no analytical lineshape has been derived

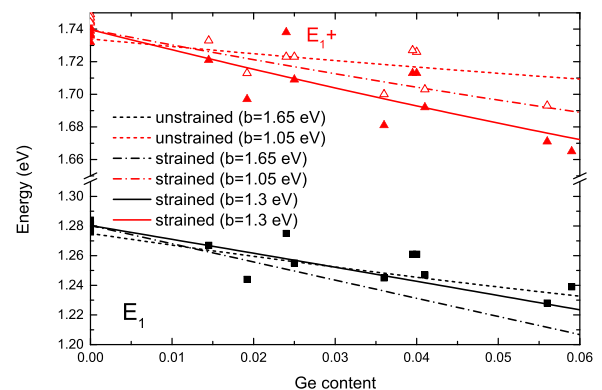


FIG. 4. E_1 and $E_1 + \Delta_1$ energies from ellipsometry (symbols) along with predictions calculated from the established bowing parameters for relaxed (dotted) and strained (dash-dotted) alloys. Our data fit best with a single bowing parameter for both CPs (solid). Closed (open) symbols show the results where both the phase angles were required to be the same (allowed to differ).

yet which could be compared with dielectric function spectra.¹⁵ Our best current theory¹⁵ attributes \bar{E}_0 to intravalence band transitions from Γ_7^- to the highest hole band (Γ_7^+ or Γ_6^+ , whatever is lower) and places the maximum of ϵ_2 approximately 30 meV (about kT) above \bar{E}_0 . We therefore subtract this value from our peak energies of ϵ_2 to determine the \bar{E}_0 energies of $\text{Sn}_{1-x}\text{Ge}_x$, see Table I.

We thus find $\bar{E}_0 = 0.418$ eV for strained α -Sn on InSb (001), which corresponds to the energy difference between Γ_7^+ and Γ_7^- (Fig. 1). To obtain the \bar{E}_0 energy for unstrained α -Sn, we must add $|\delta_0|$ (6 meV, half the Γ_8^+ splitting under [001] shear strain) and the hydrostatic shift (12 meV) to obtain the energy difference between Γ_8^+ and Γ_7^- in unstrained α -Sn, which yields 0.436 eV. (A detailed discussion of the influence of biaxial stress on the band structure can be found in the supplementary material.) We consider this value the \bar{E}_0 energy for unstrained α -Sn and enter it in Table S1. Also see Fig. 5. Our \bar{E}_0 of 0.436 eV for unstrained α -Sn is in reasonable agreement with the established value of 0.413 eV, which was determined using magnetoreflectance.¹⁸ A better agreement should not be expected due to the significant non-parabolicity of the Γ_8^+ bands (Fig. 1) and the M-shape of the Γ_7^- VB.¹⁹ Our room-temperature ellipsometry measurement probes an energy range of about 30 meV around the Γ_7^- and Γ_8^+ extrema, while magnetoreflectance¹⁸ at 1.5 K probes at much higher energies (up to 150 meV) and extrapolates downward to determine \bar{E}_0 . The \bar{E}_0 gap is independent of temperature between 1.5 and 85 K, determined from magneto-reflectance measurements,¹⁸ and not expected to change up to room temperature.¹⁵

Using photoluminescence measurements on unstrained Ge-rich $\text{Ge}_{1-x}\text{Sn}_x$ alloys,²⁰ a large bowing parameter of $b = 2.46$ eV was found for the E_0 gap, see Table S1. A recent density-functional calculation⁸ finds an even larger value of $b = 3.02$ eV. This suggests a decrease in the Γ_7^- VB energy for relaxed tin-rich $\text{Sn}_{1-x}\text{Ge}_x$ alloys with the increasing Ge content relative to the Γ_8^+ VB maximum, which would lead to an increase in the observed \bar{E}_0 energy, as shown in Fig. 5. The hydrostatic portion of the in-plane biaxial

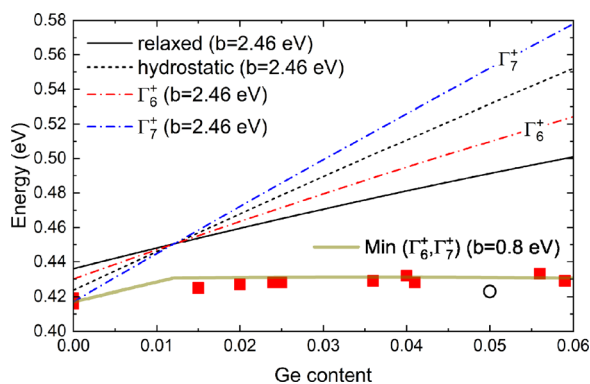


FIG. 5. \bar{E}_0 gaps of pseudomorphic $\text{Sn}_{1-x}\text{Ge}_x$ alloys on InSb (001) from infrared ellipsometry (■) in comparison with predictions using a bowing parameter of 2.46 eV for relaxed $\text{Sn}_{1-x}\text{Ge}_x$ (solid), modified by the hydrostatic volume change (dotted) and split by [001] shear strain (dash-dotted). A good fit to the experimental data requires a bowing parameter of 0.8 eV (thick line). One layer is partially relaxed (○).

stress in pseudomorphic $\text{Sn}_{1-x}\text{Ge}_x$ on InSb (001) will modify the \bar{E}_0 gap and will cause a decrease by 12 meV for pure α -Sn on InSb (001) and an increase for $\text{Sn}_{1-x}\text{Ge}_x$ alloys with $x > 1.2\%$ (by 51 meV for $x = 0.06$). Finally, the [001] shear strain splits the doubly degenerate Γ_8^+ band into non-degenerate Γ_6^+ and Γ_7^+ states. If we attribute \bar{E}_0 to intravalence band transitions from Γ_7^- to the highest hole band, then the experimentally observed \bar{E}_0 peak should follow the lower of the Γ_7^+ and Γ_6^+ energies. (Also see Fig. 1 and supplementary material.)

We observe, however, that these predictions do not agree at all with our experimental data. As the Ge content is increased up to 6%, our \bar{E}_0 energy increases by not more than 10 meV. This behavior can be described with a bowing parameter of about 0.8 eV, as shown by the thick line in Fig. 5.

In summary, we have determined the dielectric function of pseudomorphic tin-rich $\text{Sn}_{1-x}\text{Ge}_x$ alloys on InSb (001) for Ge contents up to 6% using infrared and spectroscopic ellipsometry. These measurements suggest a germanium-like band structure for such alloys, similar to the elemental endpoints. The E_1 and $E_1 + \Delta_1$ critical points (which originate from interband optical transitions along [111] and at the L -point) show a decrease with the increasing Ge content at a rate not entirely incompatible with the bowing parameters determined for Ge-rich alloys. The inverted direct bandgap \bar{E}_0 is nearly independent of the Ge content up to 6%, which suggests a bowing parameter on the order of 0.8 eV, much lower than the value of 2.46 eV determined using photoluminescence of Ge-rich alloys.

See supplementary material for the tabulated optical constants of $\text{Sn}_{1-x}\text{Ge}_x$ alloys, an interpolation scheme of inverse effective mass parameters, a discussion of the influence of biaxial stress on the valence band structure and critical points of $\text{Sn}_{1-x}\text{Ge}_x$ alloys, critical-point parameters, and characterization results for our epitaxial layers using atomic force microscopy and high-resolution x-ray diffraction.

This work was supported by the Air Force Office of Scientific Research (FA9550-16RYCOR296). R.A.C. and S.Z. acknowledge support from the AFOSR Summer Faculty Fellowship Program. We are grateful to José Menéndez for stimulating discussions. One of us (S.Z.) is grateful to the Institute of Physics, Czech Academy of Sciences, for hospitality and support in Prague, Czech Republic, where this article was revised after review.

REFERENCES

- ¹S. Groves and W. Paul, *Phys. Rev. Lett.* **11**, 194 (1963).
- ²C.-Z. Xu, Y.-H. Chan, Y. Chen, P. Chen, X. Wang, C. Dejoie, M.-H. Wong, J. A. Hlevyack, H. Ryu, H.-Y. Kee et al., *Phys. Rev. Lett.* **118**, 146402 (2017).
- ³H. Huang and F. Liu, *Phys. Rev. B* **95**, 201101 (2017).
- ⁴D. Zhang, H. Wang, J. Ruan, G. Yao, and H. Zhang, *Phys. Rev. B* **97**, 195139 (2018).
- ⁵E. A. Fitzgerald, P. E. Freeland, M. T. Asom, W. P. Lowe, R. A. Macharrie, Jr., B. E. Weir, A. R. Kortan, F. A. Thiel, Y.-H. Xie, A. M. Sergent et al., *J. Electron. Mater.* **20**, 489 (1991).
- ⁶D. Imbrenda, R. Hickey, R. A. Carrasco, N. S. Fernando, J. VanDerslice, S. Zollner, and J. Kolodzey, *Appl. Phys. Lett.* **113**, 122104 (2018).
- ⁷H.-S. Lan, S. T. Chang, and C. W. Liu, *Phys. Rev. B* **95**, 201201 (2017).

- ⁸M. P. Polak, P. Scharoch, and R. Kudrawiec, *J. Phys. D* **50**, 195103 (2017).
- ⁹N. S. Fernando, R. A. Carrasco, R. Hickey, J. Hart, R. Hazbun, S. Schoeche, J. N. Hilfiker, J. Kolodzey, and S. Zollner, *J. Vac. Sci. Technol. B* **36**, 021202 (2018).
- ¹⁰V. R. D'Costa, C. S. Cook, A. G. Birdwell, C. L. Littler, M. Canonico, S. Zollner, J. Kouvetakis, and J. Menendez, *Phys. Rev. B* **73**, 125207 (2006).
- ¹¹V. R. D'Costa, W. Wang, Q. Zhou, E. S. Tok, and Y. C. Yeo, *Appl. Phys. Lett.* **104**, 022111 (2014).
- ¹²L. Viña, H. Höchst, and M. Cardona, *Phys. Rev. B* **31**, 958 (1985).
- ¹³R. F. C. Farrow, D. S. Robertson, G. M. Williams, A. G. Cullis, G. R. Jones, I. M. Young, and P. N. J. Dennis, *J. Cryst. Growth* **54**, 507 (1981).
- ¹⁴C. A. Hoffman, J. R. Meyer, R. J. Wagner, F. J. Bartoli, M. A. Engelhardt, and H. Höchst, *Phys. Rev. B* **40**, 11693 (1989).
- ¹⁵R. A. Carrasco, C. M. Zamarripa, S. Zollner, J. Menéndez, S. Chastang, J. Duan, G. J. Grzybowski, B. B. Claflin, and A. M. Kiefer, *Appl. Phys. Lett.* **113**, 232104 (2018).
- ¹⁶C. Xu, C. Senaratne, R. J. Culbertson, J. Kouvetakis, and J. Menéndez, *J. Appl. Phys.* **122**, 125702 (2017).
- ¹⁷P. Y. Yu and M. Cardona, *Fundamentals of Semiconductors* (Springer, Heidelberg, 2010).
- ¹⁸S. H. Groves, S. C. Pidgeon, A. W. Ewald, and R. J. Wagner, *J. Phys. Chem. Solids* **31**, 2031 (1970).
- ¹⁹A. Barfuss, L. Dudy, M. R. Scholz, H. Roth, P. Höpfner, C. Blumenstein, G. Landolt, J. H. Dil, N. C. Plumb, M. Radovic, *et al.*, *Phys. Rev. Lett.* **111**, 157205 (2013); **112**, 239903 (2014).
- ²⁰L. Jiang, J. D. Gallagher, C. L. Senaratne, T. Aoki, J. Mathews, J. Kouvetakis, and J. Menendez, *Semicond. Sci. Technol.* **29**, 115028 (2014).

Supplementary Material:

Dielectric function and band structure of $\text{Sn}_{1-x}\text{Ge}_x$ ($x < 0.06$) alloys on InSb

(Dated: 17 January 2019)

Rigo A. Carrasco,¹ Stefan Zollner,¹ Stephanie A. Chastang,² Jinsong Duan,² Gordon J. Grzybowski,² Bruce B. Claffin,³ and Arnold M. Kiefer³

¹*Department of Physics, New Mexico State University, P.O. Box 30001, Las Cruces, NM 88003*

²*KBRwyle, 2601 Mission Point Blvd., Suite 300, Dayton, OH 45431*

³*Air Force Research Laboratory, Sensors Directorate, Wright-Patterson Air Force Base, OH 45433*

S1. VALENCE BAND WARPING IN $\text{SN}_{1-x}\text{GE}_x$ ALLOYS

Warping of the Γ_8^+ p-bonding orbitals is of critical importance in $\text{Sn}_{1-x}\text{Ge}_x$ alloys, especially under a biaxial in-plane stress. In a very simple $\vec{k}\cdot\vec{p}$ model, this warping is described by three inverse effective mass parameters¹⁷ (Dresselhaus 1955)

$$A = 1 - \frac{2}{3} \left(\frac{P^2}{m_0 E_0} + \frac{2Q^2}{m_0 E'_0} \right), \quad (\text{S1})$$

$$B = \frac{2}{3} \left(\frac{-P^2}{m_0 E_0} + \frac{Q^2}{m_0 E'_0} \right), \quad (\text{S2})$$

$$C^2 = \frac{16P^2 Q^2}{3m_0^2 E_0 E'_0}, \quad (\text{S3})$$

expressed in units of $\hbar^2/2m_0$, where m_0 is the free electron mass, P and Q are the momentum matrix elements connecting the Γ_{25}' band with the Γ_2' and Γ_{15} bands, respectively, and E_0 and E'_0 the corresponding direct band gaps at the Γ -point.

In Ge, $A=-13.38$ is negative, because the term in parentheses in Eq. (S1) is much larger than one. $B=-8.5$ is also negative, because $E_0 < E'_0$ in Eq. (S2); and finally $C^2=173$ is positive, because all parameters in Eq. (S3) are positive. In α -tin, $A=19.2$ is positive, because E_0 is negative and its magnitude is less than E'_0 . $B=26.3$ is positive, because E_0 is negative and all other factors are positive. For the same reason C^2 is negative. (For Ge, the values of the inverse effective mass parameters are not controversial and were taken from Yu and Cardona,¹⁷ Table 2.24. We adopted values for α -tin measured using angle-dependent Shubnikov-de Haas experiments by Booth and Ewald 1968, which are different from calculated inverse effective mass parameters, for example Cardona 1963, Cardona 1967, Lawaetz 1971, or Leung and Liu 1973. Different conventions for signs and units of these parameters are common.)

If we introduce $E_P=2P^2/m_0$ and $E_Q=2Q^2/m_0$ and stress that the inverse effective mass parameters depend

on composition, we can rewrite Eqs. (S1-S3) as

$$A(x) = 1 - \frac{E_P(x)}{3E_0(x)} - \frac{2E_Q(x)}{3E'_0(x)}, \quad (\text{S4})$$

$$B(x) = -\frac{E_P(x)}{3E_0(x)} + \frac{E_Q(x)}{3E'_0(x)}, \quad (\text{S5})$$

$$C^2(x) = \frac{4E_P(x)E_Q(x)}{3E_0(x)E'_0(x)}. \quad (\text{S6})$$

In $\text{Sn}_{1-x}\text{Ge}_x$ alloys, all three parameters A , B , and C^2 will diverge as E_0 crosses from negative to positive values with increasing x . The associated effective masses¹⁷

$$\vec{k} \parallel [100] \quad \frac{1}{m_{\text{hh}}} = -A + B \quad (\text{S7})$$

$$\frac{1}{m_{\text{lh}}} = -A - B \quad (\text{S8})$$

$$\vec{k} \parallel [111] \quad \frac{1}{m_{\text{hh}}} = -A + B \sqrt{1 + \frac{C^2}{3B^2}} \quad (\text{S9})$$

$$\frac{1}{m_{\text{lh}}} = -A - B \sqrt{1 + \frac{C^2}{3B^2}} \quad (\text{S10})$$

will become very small at this cross-over and the Γ_8^+ bands will take a very large curvature for small wave vectors \vec{k} . The divergence is caused by the increased interactions (repulsion) of the Γ_7^- and Γ_8^+ bands with small energy denominators in $\vec{k}\cdot\vec{p}$ theory.

Because of this divergence, it is completely inappropriate to attempt a linear interpolation of the inverse effective mass parameters with tin content. Instead, we note that the matrix elements E_P and E_Q are similar for Ge and tin and therefore should tolerate a linear interpolation (Lawaetz 1971). We also know the dependence of the direct band gaps E_0 and E'_0 on composition (including quadratic bowing for some gaps,^{9,12} Viña 1984) and we might want to calculate composition-dependent inverse effective mass parameters using Eqs. (S4-S6). The problem is, of course, that we are attempting to predict three parameters A , B , and C^2 with only two variables E_P and E_Q , since the energies E_0 and E'_0 are known from spectroscopic measurements. We address this dilemma by introducing an artificial third parameter E_{PQ} , which should be similar to the product of E_P and E_Q :

$$A(x) = 1 - \frac{E_P(x)}{3E_0(x)} - \frac{2E_Q(x)}{3E'_0(x)}, \quad (\text{S11})$$

$$B(x) = -\frac{E_P(x)}{3E_0(x)} + \frac{E_Q(x)}{3E'_0(x)}, \quad (\text{S12})$$

$$C^2(x) = \frac{4E_{PQ}(x)}{3E_0(x)E'_0(x)}. \quad (\text{S13})$$

We now have three equations and three unknowns, which

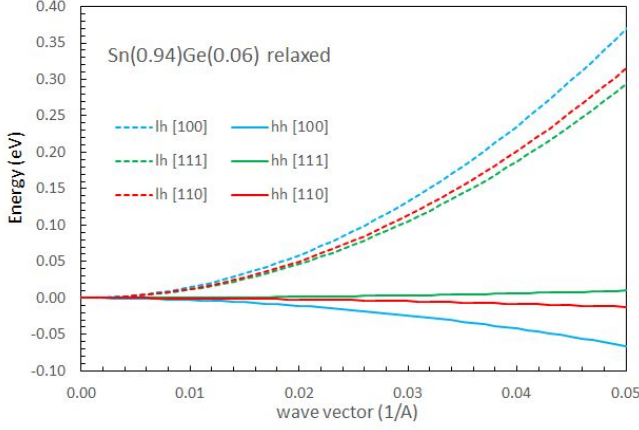


FIG. S1. Warped (unstrained) Γ_8^+ bands of $\text{Sn}_{0.94}\text{Ge}_{0.06}$ calculated from the inverse effective mass parameters in Table SI along high-symmetry directions. The light and heavy “hole” bands are shown by dashed and solid lines, respectively.

are easy to solve:

$$E_P = E_0(1 - A - 2B), \quad (\text{S14})$$

$$E_Q = E'_0(1 - A + B), \quad (\text{S15})$$

$$E_{PQ} = \frac{3}{4}E_0E'_0C^2. \quad (\text{S16})$$

In conclusion, to determine the inverse effective mass parameters A , B , and C^2 as a function of Ge content x , we start with their values for the elements listed in Table SI. We then calculate E_P , E_Q , and E_{PQ} for the elements using Eqs. (S14-S16) and interpolate them linearly with composition (Lawaetz 1971). Finally, we use Eqs. (S11-S13) to find the inverse effective mass parameters for the alloys. From A , B , and C^2 , we can also calculate the Luttinger (1956) parameters and the average isotropic effective masses from¹⁷ (Persson 2001)

$$m_{hh, lh}^{-1} = A \pm |B| \sqrt{1 + C^2/5B^2}. \quad (\text{S17})$$

(We believe that this corrected equation was the intent of Yu and Cardona.¹⁷ The factor 3/15 can be obtained by writing the Dresselhaus-Kip-Kittel expression in polar coordinates and integrating over the unit sphere with certain approximations.) This expression works very well for Si and Ge, but only for the light “hole” mass of α -tin. The average heavy hole mass of α -tin and tin-rich $\text{Sn}_{1-x}\text{Ge}_x$ alloys comes out much too large.

This interpolation is shown in Table SI. Results for E_P and E_Q of Ge and Sn are quite reasonable (Lawaetz 1971) and E_{PQ} is within a factor of two of the product $E_P E_Q$. Figure S1 shows the warped Γ_8^+ bands of unstrained $\text{Sn}_{1-x}\text{Ge}_x$ ($x=0.06$) for small wave vectors in high-symmetry directions. The results are similar to α -Sn,¹⁵ including the positive (electron-like) curvature of the heavy hole for wave vectors along the [111] directions.

TABLE SI. Important material parameters for Sn, Ge, and $\text{Sn}_{1-x}\text{Ge}_x$ alloys (at room temperature) and their interpolation. An example is given for an alloy with $x=0.06$. Units in parenthesis. $b(\text{GeSn})$ is the bowing parameter. We do not interpolate the elastic constants C_{11} and C_{12} , only their ratio. Interpolation of inverse effective mass parameters A , B , and C^2 is described in the supplemental materials. Most parameters from Ref. 9 (except where noted).

	Ge	Sn	$b(\text{GeSn})$	alloy (6%)
a (Å)	5.658	6.489	0	6.439
C_{11} (GPa)	128.5	69.0	NA	NA
C_{12} (GPa)	48.3	29.3	NA	NA
C_{12}/C_{11}	0.376	0.425	0	0.422
E_1 (eV)	2.120	1.275 ^a	1.65	1.233
E_1 (eV) ^b	2.120	1.275	1.35	1.250
$E_1 + \Delta_1$ (eV)	2.310	1.734 ^a	1.05	1.709
$E_1 + \Delta_1$ (eV) ^b	2.310	1.734	1.35	1.692
Δ_1 (eV)	0.190	0.459 ^a	-0.60	0.477
Δ_1 (eV) ^b	0.190	0.459	0	0.443
E_0 (eV)	0.796	-0.436 ^a	2.46	-0.501
E_0 (eV) ^b	0.796	-0.436	0.8	-0.407
$E_0 + \Delta_0$ (eV)	1.096	0.364	3.04	0.236
Δ_0 (eV)	0.30	0.8	0.58	0.737
E'_0 (eV)	3.1 ^c	2.4 ^d	0	2.44
A ($\hbar^2/2m_0$)	-13.38	19.2	NA	15.9 ^e
B ($\hbar^2/2m_0$)	-8.5	26.3	NA	22.8 ^e
C^2 ($\hbar^4/4m_0^2$)	173	-1100	NA	-898 ^e
E_P (eV)	25.0	29.2	0	29.0
E_Q (eV)	18.2	19.4	0	19.4
E_{PQ} (eV ²)	320	818	0	788
$a(E_0)$ (eV)	-9.5 ^f	-7.0 ^g	0	-7.2
$b(\Gamma_8^+)$ (eV)	-1.9 ^h	-2.3 ⁱ	0	-2.3

^a Ref. 15.

^b This work.

^c Viña 1984.

^d Ref. 12.

^e Calculated using Eqs. (S11-S13).

^f C.G. Van de Walle, Phys. Rev. B **39**, 1871 (1989).

^g T. Brudevoll, D.S. Citrin, M. Cardona, and N.E. Christensen, Phys. Rev. B **48**, 8629 (1993).

^h J. Liu, D.D. Cannon, K. Wada, Y. Ishikawa, D.T. Danielson, S. Jongthammanurak, J. Michel, and L. Kimerling, Phys. Rev. B **70**, 155309 (2004).

ⁱ Ref. 14.

S2. STRESS AND STRAIN IN $\text{Ge}_{1-x}\text{Sn}_x$ ALLOYS

For pseudomorphic growth of α -Sn or $\text{Sn}_{1-x}\text{Ge}_x$ alloys on InSb (001), the in-plane lattice constant a_{\parallel} is equal to that of the substrate a_S (pseudomorphic condition). This creates a biaxial stress along the surface of the wafer described by a stress tensor

$$\mathbf{X} = \begin{pmatrix} X & 0 & 0 \\ 0 & X & 0 \\ 0 & 0 & 0 \end{pmatrix}. \quad (\text{S18})$$

(There is no stress along the growth direction, defined as the z -axis.) This biaxial stress is related to a strain

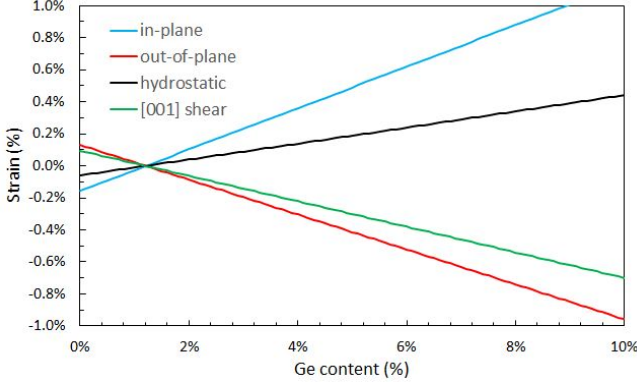


FIG. S2. In-plane, out-of-plane, hydrostatic, and [001] pure shear strain as a function of Ge content x for $\text{Sn}_{1-x}\text{Ge}_x$ alloys grown pseudomorphically on InSb (001).

tensor (Cardona & Christensen 1987)

$$\begin{pmatrix} \epsilon_{\parallel} & 0 & 0 \\ 0 & \epsilon_{\parallel} & 0 \\ 0 & 0 & \epsilon_{\perp} \end{pmatrix} = \epsilon_H \begin{pmatrix} 1 & 0 & 0 \\ 0 & 1 & 0 \\ 0 & 0 & 1 \end{pmatrix} + \epsilon_S \begin{pmatrix} -1 & 0 & 0 \\ 0 & -1 & 0 \\ 0 & 0 & 2 \end{pmatrix} \quad (\text{S19})$$

with perpendicular (out-of-plane) and parallel (in-plane) components ϵ_{\perp} and ϵ_{\parallel} . ϵ_H and ϵ_S are the hydrostatic and [001] pure shear strain components¹⁷ (Cardona & Christensen 1987)

$$\epsilon_H = \frac{1}{3}(\epsilon_{\perp} + 2\epsilon_{\parallel}) \quad \text{and} \quad \epsilon_S = \frac{1}{3}(\epsilon_{\perp} - \epsilon_{\parallel}). \quad (\text{S20})$$

The in-plane strain is defined as

$$\epsilon_{\parallel} = \frac{\Delta a}{a(x)} = \frac{a_S - a(x)}{a(x)}, \quad (\text{S21})$$

where $a(x)$ is the (cubic) lattice constant of the unstrained $\text{Sn}_{1-x}\text{Ge}_x$ alloy. Negative strain indicates a reduction of the lattice parameter (compressive strain), while a positive strain indicates an increase of the lattice parameter (tensile strain). Strain is usually a small dimensionless number stated as a percentage. Growth of α -Sn on InSb ($x=0$) results in compressive (negative) in-plane strain. The magnitude of this in-plane strain decreases with increasing x in $\text{Sn}_{1-x}\text{Ge}_x$ alloys and vanishes for $x \approx 1.2\%$. For larger x , the in-plane strain becomes tensile, see Fig. S2.

The cubic (bulk) unit cell deforms tetragonally and the perpendicular (out-of-plane) lattice constant of the epitaxial layer measured with symmetric (004) high-resolution x-ray diffraction becomes

$$a_{\perp} = (1 + \epsilon_{\perp}) a(x), \quad (\text{S22})$$

where the out-of-plane strain (Cardona & Christensen 1987)

$$\epsilon_{\perp} = -2 \frac{C_{12}}{C_{11}} \epsilon_{\parallel} = -\frac{2\nu}{1-\nu} \epsilon_{\parallel} \quad (\text{S23})$$

is calculated using the elastic constants C_{ij} (see Table SI) or the Poisson ratio $\nu = C_{12}/(C_{11} + C_{12}) = 0.30$.

Figure S2 shows the in-plane, out-of-plane, hydrostatic, and [001] shear strain components for $\text{Sn}_{1-x}\text{Ge}_x$ alloys on InSb (001). We see clearly how the in-plane strain changes sign as a function of x . While the in-plane strain is compressive for pure α -Sn ($x=0$), it becomes tensile for $x > 1.2\%$. The in-plane and out-of-plane strain have opposite signs. The hydrostatic strain has the same sign as the in-plane strain, but is much smaller. The [001] shear strain has the same sign as the out-of-plane strain.

S3. RESPONSE OF VALENCE BANDS TO STRAIN

The strain described above for $\text{Sn}_{1-x}\text{Ge}_x$ alloys on InSb (001) splits the Γ_8^+ bands and either creates a Dirac-crossing of the heavy and light “hole” bands (for $x < 1.2\%$) or opens a gap $2\delta_0$ (for $x > 1.2\%$), as shown in Fig. 1. The dispersion of the strained bands can be described within Pikus-Bir (1959) theory (Hoffmann 1989) by

$$E_{\pm} = Ak^2 \pm [B^2k^4 + C^2(k_x^2k_y^2 + k_x^2k_z^2 + k_y^2k_z^2) + B\delta_0(2k_z^2 - k_x^2 - k_y^2) + \delta_0^2]^{\frac{1}{2}}, \quad (\text{S24})$$

where $\delta_0 = 3b\epsilon_S$ is half the strain splitting of the Γ_8^+ bands, b the deformation potential listed in Table SI, and ϵ_S the pure (traceless) shear component of the strain.

As an example, we show the Γ_8^+ bands for small wave vectors in Fig. 1. In the compressive in-plane case shown in Fig. 1(c) for $x < 1.2\%$, the heavy and light “hole” bands have the expected curvature (downward and upward, respectively) for wave vectors perpendicular to the [001] shear strain, but they curve in the opposite direction for wave vectors parallel to the [001] shear strain and cross at the so-called Dirac point. At 0 K, electronic states below the Dirac point are filled, while those above it are empty. In the tensile in-plane case shown in Fig. 1(d) for $x > 1.2\%$, the heavy and light “hole” bands are nearly parabolic and show the expected curvature (upward or downward) for wave vectors oriented parallel to the [001] shear strain axis. In the other directions, however, there is a significant non-parabolicity. The heavy hole band first curves upward and only turns to negative energies for larger wave vectors. This was first treated by Cardona (1967) and is described in more detail in Ref. 15. $\text{Sn}_{1-x}\text{Ge}_x$ alloys on InSb ($x > 1.2\%$) are indirect semiconductors with a small band gap, because the VB maximum does not occur exactly at the Γ -point. Current MBE growth techniques can achieve Ge contents up to about 6% in pseudomorphic $\text{Sn}_{1-x}\text{Ge}_x$ alloys on InSb (001), which leads to a Γ_8^+ splitting of about 50 meV. See Ref. 15 (supplemental materials) for additional detail.

S4. RESPONSE OF \bar{E}_0 GAP TO STRAIN

The \bar{E}_0 gap separates the Γ_7^- valence band from the Γ_8^+ state. The [001] shear portion of the strain splits this gap due to the splitting of the Γ_8^+ states given by Eq. (S24). In addition, the hydrostatic portion of the strain changes the Γ_7^- energy by $3a\epsilon_H$, where a is the hydrostatic deformation potential for the \bar{E}_0 gap given in Table SI. a has a negative value of about -7 eV. For the compressive in-plane strain of α -Sn on InSb (001), ϵ_H is negative and therefore Γ_7^- moves up by about 12 meV, which decreases the \bar{E}_0 gap compared to unstrained α -Sn by the same amount. On the other hand, in $\text{Sn}_{1-x}\text{Ge}_x$ alloys with $x > 1.2\%$, the tensile in-plane strain causes a hydrostatic expansion ($\epsilon_H < 0$), which increases \bar{E}_0 (by 51 meV for $x=6\%$) relative to a relaxed alloy with the same composition, see Fig. 5.

S5. RESPONSE OF E_1 AND $E_1 + \Delta_1$ CRITICAL POINT ENERGIES TO STRAIN

The dependence of the E_1 and $E_1 + \Delta_1$ critical points (see Fig. 1) on composition for unstrained (relaxed) $\text{Sn}_{1-x}\text{Ge}_x$ alloys was calculated using Eq. (1) with the parameters given in Table SI. The spin-orbit splitting Δ_1 of the VB at the L point is taken as the difference between the E_1 and $E_1 + \Delta_1$ energies with parameters in Table SI. Note the bowing for Δ_1 , which is common for semiconductor alloys¹⁰ (Logothetidis 1991). Under a biaxial in-plane stress, the energies are⁹

$$E_1^s = E_1^0 + \frac{1}{2}\Delta_1 + \Delta E_H - \sqrt{\frac{1}{4}(\Delta_1)^2 + (\Delta E_S)^2}, \quad (\text{S25})$$

$$(E_1 + \Delta_1)^s = (E_1 + \Delta_1)^0 - \frac{1}{2}\Delta_1 + \Delta E_H + \sqrt{\frac{1}{4}(\Delta_1)^2 + (\Delta E_S)^2}, \quad (\text{S26})$$

where the superscripts s and 0 denote the band gaps of the strained and relaxed alloys, respectively. ΔE_H and ΔE_S are the energy shifts due to hydrostatic and [001] shear strain, respectively, calculated using

$$\Delta E_H = \sqrt{3}D_1^1\epsilon_H \quad \text{and} \quad \Delta E_S = \sqrt{6}D_3^3\epsilon_S, \quad (\text{S27})$$

where $D_1^1 = -5.4$ eV and $D_3^3 = -3.8$ eV are the hydrostatic and shear deformation potentials for $\text{Ge}_{1-y}\text{Sn}_y$ alloys taken from D'Costa (2014), which is significantly lower than for bulk Ge. The sign of D_3^3 affects the intensities of the two critical points and therefore we follow the sign convention of Pantelides & Zollner (2002).

We previously¹⁵ determined the strained values $E_1^s = 1.280$ eV and $(E_1 + \Delta_1)^s = 1.739$ eV with $\epsilon_H = -0.06\%$ and $\epsilon_S = 0.10\%$ from ellipsometry of pseudomorphic α -Sn on InSb (001). This yields the unstrained values $E_1^0 = 1.275$ eV and $(E_1 + \Delta_1)^0 = 1.734$ eV, as shown in Table SI. For such a small shear strain (for $x=0$) and the large spin-orbit splitting Δ_1 , the shear

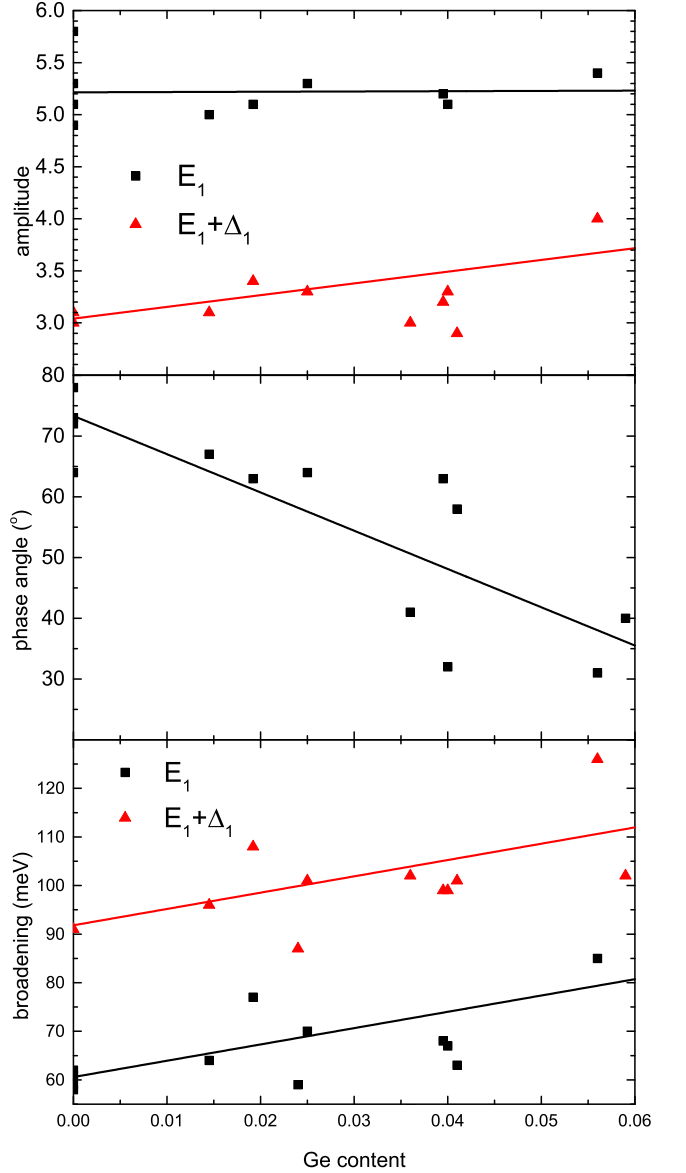


FIG. S3. Amplitudes, broadenings, and phase angles for the E_1 and $E_1 + \Delta_1$ critical points versus Ge content determined from spectroscopic ellipsometry (symbols). The straight lines show the best linear fit.

splitting under the square root of Eqs. (S25-S26) can be ignored and only the hydrostatic shift ΔE_H contributes. The shear contribution ΔE_S becomes measurable for larger x near 5%.

S6. AMPLITUDES, BROADENINGS, AND PHASE ANGLES FOR E_1 AND $E_1 + \Delta_1$ CRITICAL POINTS

The parameters used to describe the E_1 and $E_1 + \Delta_1$ critical points, see Eq. (2), are the amplitude A , energy E , broadening Γ , and phase angle ϕ . It is customary to use the same phase angle for E_1 and $E_1 + \Delta_1$. The en-

ergies, broadenings, and phase angles are listed in Table I. The energies are plotted in Fig. 4 and discussed in the main text. Figure S3 shows the amplitudes, broadenings, and phase angles as a function of Ge content. Compare Ref. 9 for a similar discussion of pseudomorphic Ge-rich $\text{Ge}_{1-x}\text{Sn}_x$ alloys on Ge.

Our broadenings are comparable to, or perhaps a bit smaller than those reported in Ref. 12, indicating the high quality of our epilayers. They increase with Ge content at a rate of 0.34 eV, as shown by the straight lines, due to alloy scattering. The phase angle decreases from 70° for pure α -Sn to 32° for $\text{Ge}_{0.94}\text{Sn}_{0.06}$ at a rate of 6.3° per atomic percent Ge. Increased alloy scattering in disordered alloys reduces the excitonic enhancement of the E_1 critical point and therefore ϕ decreases with increasing Ge content⁹ (Logothetidis 1991) to values below 90° .

The amplitudes of E_1 and $E_1 + \Delta_1$ show interesting trends. While the E_1 amplitude is nearly constant at 5.2 ± 0.2 , the $E_1 + \Delta_1$ amplitude increases linearly at a rate of 0.11 per atomic percent Ge. According to $\vec{k} \cdot \vec{p}$ theory, the [001] pure shear strain changes the amplitudes of these critical points as a function of shear strain ϵ_S by (Pantelides and Zollner 2002)

$$\Delta A(\epsilon_S)/A_0 = \pm \sqrt{6} D_3^3 \epsilon_S / \Delta_1, \quad (\text{S28})$$

where the + sign is for the $E_1 + \Delta_1$ amplitude and the - sign for the E_1 amplitude. A_0 is the amplitude of the CPs in relaxed alloys. For $x > 1.2\%$, both the shear strain and the deformation potential $D_3^3 = -3.8$ eV are negative and therefore the amplitude of E_1 should decrease and that of $E_1 + \Delta_1$ should increase with increasing Ge content (and thus increasing magnitude of the compressive [001] shear strain). The relative rate of change calculated from Eq. (S28) is 0.02 per atomic percent Ge, which corresponds to a decrease of the E_1 amplitude at a rate of 0.1 and an increase of the $E_1 + \Delta_1$ amplitude at a rate of 0.06 (per atomic percent Ge). As shown in Fig. S3, we do not observe the expected decrease of the E_1 amplitude, but the observed increase of the $E_1 + \Delta_1$ amplitude is twice as large as predicted.

The absolute values of the amplitudes for relaxed alloys are given by^{12,15}

$$A_{E_1} = 44 \frac{E_1 + \frac{1}{3} \Delta_1}{a E_1^2}, \quad (\text{S29})$$

$$A_{E_1 + \Delta_1} = 44 \frac{E_1 + \frac{2}{3} \Delta_1}{a (E_1 + \Delta_1)^2}, \quad (\text{S30})$$

where a is the lattice constant of the alloy in \AA and energies are in eV. For pure α -tin we calculated amplitudes of 5.9 and 3.6 for E_1 and $E_1 + \Delta_1$, respectively, see Ref. 15, in excellent agreement with our experiments, see Fig. S3. The agreement of our experiment with this theory for uncorrelated electron-hole pairs indicates that the excitonic contribution to the E_1 and $E_1 + \Delta_1$ critical points is weak in α -Sn and smaller than in other materials like Si, GaAs, or GaSb.¹⁵

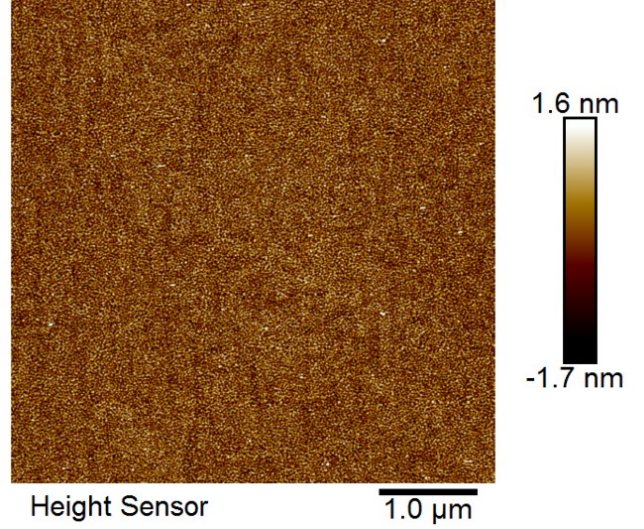


FIG. S4. Atomic force micrograph ($5 \times 5 \mu\text{m}^2$ scan range) of a $\text{Sn}_{1-x}\text{Ge}_x$ alloy on InSb (001) with $x=0.059$ and 75 nm thickness. The rms roughness is 0.5 nm.

S7. EPILAYER CHARACTERIZATION

Atomic force micrographs with $5 \times 5 \mu\text{m}^2$ scan range were taken for selected $\text{Sn}_{1-x}\text{Ge}_x$ epilayers on InSb (001). The rms roughness was usually on the order of 0.5 nm. No misfit dislocation networks due to stress relaxation were seen. Some layers showed β -tin defects. A typical AFM image for a layer with $x=0.059$ and 75 nm thickness is shown in Fig. S4. Since the roughness is very small (0.5 nm rms), it can be neglected in the analysis of ellipsometry data, where only the native oxide was considered.

S8. LAYER ANALYSIS USING X-RAY DIFFRACTION

To assess the strain within the films, we measured each $\text{Sn}_{1-x}\text{Ge}_x$ epilayer using a PANalytical Empyrean x-ray diffractometer configured with a monochromatic $\text{Cu K}\alpha_1$ line source (1.540598\AA) and triple-axis analyzer crystal. For the purpose of demonstration, a highly strained film with 5.5% Ge is analyzed below because it represents an extreme case. Lower compositions display nearly ideal characteristics.

A symmetric 2θ - ω scan was performed near the InSb (004) peak for each epilayer. The data were then modeled using full dynamical diffraction theory (PANalytical Epitaxy and Smoothfit software) to provide film composition and film thickness (for example, see Fig. S5). The software uses Vegard's Law (1) without bowing ($b=0$) to determine film composition, with parameters given in Table SI. See also Kiefer (2017). Though the model shown in Fig. S5 follows the measured peak positions well, the intensity profile fits relatively poorly compared to the other samples in the set with lower Ge compositions. The

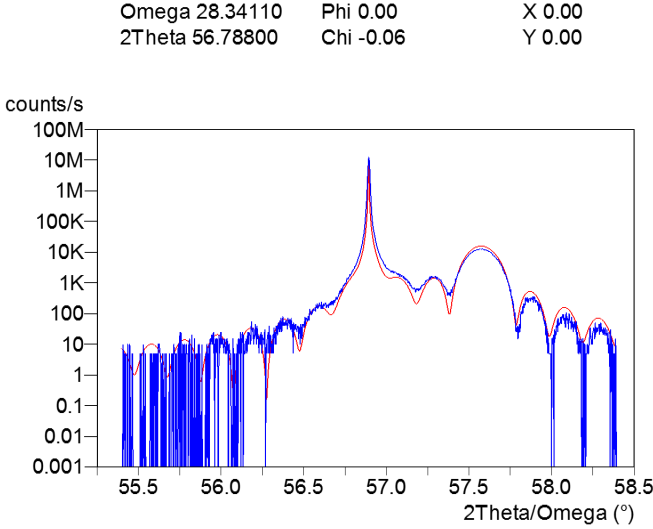


FIG. S5. (Color online) A 2θ - ω scan of a $\text{Sn}_{0.945}\text{Ge}_{0.055}$ film (50 nm thickness) on an InSb (001) substrate (blue) at the (004) Bragg reflection with an overlay of a single-layer model simulation (red). The *Pendellösung* “fringe” peaks correspond to the film thickness.

intensity mismatch may indicate potential relaxation or inhomogeneous composition as discussed below.

Additionally, rocking curves (ω -scans with fixed 2θ) centered on the (004) substrate and film peaks were measured to qualitatively determine film relaxation. (Films with epilayer peaks overlapping the substrate peak could not be measured separately.) Film-peak broadening greater than the substrate-peak breadth often indicates a dislocation density beyond that inherited from the substrate. A typical FWHM for an InSb (004) substrate peak is less than 0.004° ($\sim 14''$), near the limit of instrument resolution ($12''$). Each film has a peak FWHM the same or nearly the same as the substrate peak, implying a high degree of crystallinity; however, diffuse broadening appears around peaks of $\text{Sn}_{1-x}\text{Ge}_x$ epilayers with Ge compositions $x > 5\%$ (Fig. S6), from which we infer the onset of film relaxation by dislocation formation and glide.

Under the assumption of fully-coherent pseudomorphic growth, the film’s strain state can be adequately assessed using only the symmetric (004) 2θ - ω scan and knowledge of the film’s and substrate’s “bulk” lattice constants and elastic properties. Any strain relaxation, however, shifts the film peak with respect to the substrate peak, causing misinterpretation of the alloy composition. To avoid this ambiguity, we measure the in-plane and out-of-plane lattice constants using asymmetric Bragg reflections, *i.e.* the atomic planes are tilted away from the substrate normal. A conventional approach is to record the diffracted intensity around these asymmetric points in a reciprocal space map (RSM).

An RSM is a section of the diffraction plane corresponding physically to the plane containing the source beam and detector acceptance angle in real space. The

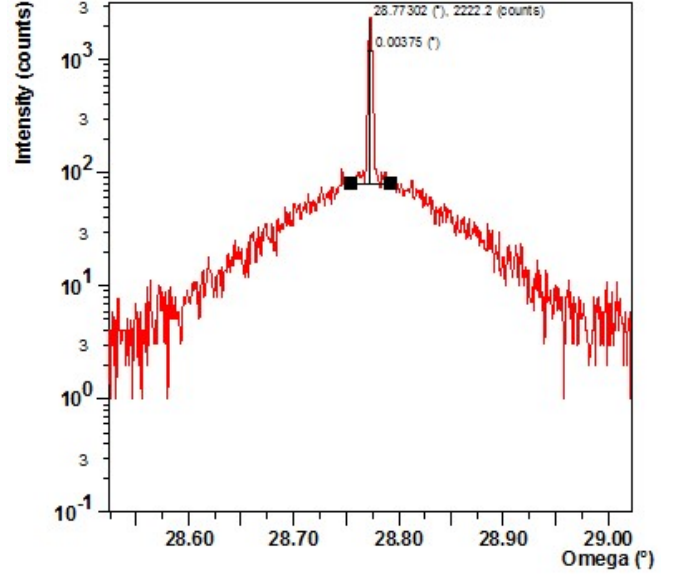


FIG. S6. (Color online) Rocking curve (ω -scan) of the epilayer peak from a $\text{Sn}_{0.945}\text{Ge}_{0.055}$ film (50 nm) on a InSb (001) substrate plotted on a logarithmic scale. Though the FWHM of the film peak is very narrow, broad diffuse-scattering is evident near the peak’s base.

diffractometer is aligned so the diffraction plane passes through the reflections of interest. Several linear scans, either 2θ vs. ω or 2θ - ω vs. ω , comprise an intensity map $I(\omega, 2\theta)$ that is represented as a reciprocal space map $I(q_{\parallel}, q_{\perp})$ using the following transformation (Fewster, 2003):

$$q_{\parallel} = [\cos(\omega) - \cos(2\theta - \omega)] / \lambda, \quad (\text{S31})$$

$$q_{\perp} = [\sin(\omega) + \sin(2\theta - \omega)] / \lambda. \quad (\text{S32})$$

The measured angular relations $I(\omega, 2\theta)$ are thus transformed into a Euclidean vector space $I(q_{\parallel}, q_{\perp})$, allowing for convenient data analysis. The reciprocal lattice of a crystal structure with orthorhombic symmetry or higher is particularly easy to analyze. The normal vectors of the atomic planes in real space correspond to the reciprocal space vectors such that the angular measurements between planes are preserved under transformation. For a crystal oriented with the (001) surface normal to the diffraction plane and the [110] in-plane direction within the diffraction plane, $\vec{q}_{\perp} = \vec{q}_{001}$ and $\vec{q}_{\parallel} = \vec{q}_{110}$. Using Bragg’s law, the length of a reciprocal space vector is related to the distance d between planes: $|\vec{q}| = 1/d = 2 \sin \theta / \lambda$. Linear distances in real space can then be read directly from the RSM. The reciprocal lattice vectors may be cast in absolute units ($1/\text{\AA}$) or in dimensionless units of $\lambda/2d$. We choose the latter in the following analysis.

The (004) RSMs were compiled using 2θ - ω scans with step sizes of 0.01° for 2θ and incrementing ω by 0.01° after each scan; the (335) RSMs by using 2θ scans with step sizes of 0.02° and increments of ω by 0.02° after each

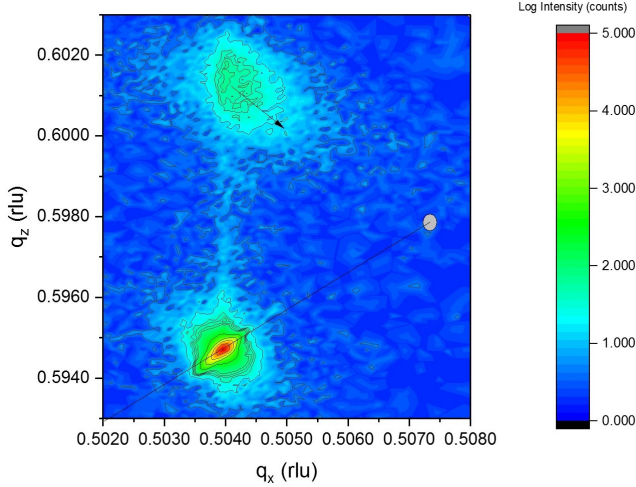


FIG. S7. (Color online) A (335) reciprocal space map of a $\text{Sn}_{0.945}\text{Ge}_{0.055}$ film (50nm) on a InSb (001) substrate. The q_x and q_z axes are parallel to the [110] and [001] directions, respectively, plotted in dimensionless reciprocal lattice units of $\lambda/2d$ and \log_{10} intensity. The dot represents the theoretical location of a fully-relaxed film and the arrow the direction of relaxation.

scan. For purposes of display, a single (335) RSM with higher resolution (0.01° step sizes) and longer counting time per step was taken and is shown in Fig. S7. Peak positions were determined using the software's built-in peak-finding algorithm. The measured peak positions of reciprocal lattice points (RLPs) of the substrate and $\alpha\text{-Sn}_{0.945}\text{Ge}_{0.055}$ film (50 nm) in the orthogonal [110] ($\phi=0^\circ$) and $[\bar{1}\bar{1}0]$ ($\phi=90^\circ$) zones are shown in Table SII. Measurement in two orthogonal zones allows substrate miscut and film lattice-tilt to be assessed. As the InSb (001) substrates are nominally cut on-axis, the analysis below confirms that the lattice tilt with respect to the goniometer axis is $<0.2^\circ$ and is negligible; therefore, we can disregard possible asymmetric strain effects.

As Fig. S7 demonstrates, the in-plane lattice constants of the substrate and film are nominally the same. The film's peak width (Δq_x) is 2 to 3 times greater than the substrate peak, and the presence of diffuse scattering in the vicinity of the film peak indicates the onset of plastic relaxation and/or compositional variation. From this cursory analysis, we conclude the film is coherent to the substrate and elastically strained.

More rigorously, we derive the lattice constants from the RLPs. The analysis can be done by various methods. We choose the straightforward method of deriving the lattice constants of the unit cell from the measured RLPs. Each RLP, $\vec{G}_{(hkl)}$, represents a linear combination of basis vectors $\{\vec{q}_x, \vec{q}_y, \vec{q}_z\}$ in the laboratory reference frame. Measuring at least two non-coplanar RLPs along two different azimuths (ϕ) provides enough information to determine a complete set of basis vectors; additional points allow a least-squares determination of the basis vectors, as in our case.

Let $\vec{G}_m = h_m \vec{q}_x + k_m \vec{q}_y + l_m \vec{q}_z$ and $\vec{q}_n = q_{n1} \hat{e}_1 + q_{n2} \hat{e}_2 + q_{n3} \hat{e}_3$, where $n \in \{x, y, z\}$ and the orthonormal vectors $\{\hat{e}_1, \hat{e}_2, \hat{e}_3\}$ correspond to the laboratory reference frame. In matrix notation,

$$\begin{pmatrix} G_{11} & G_{12} & G_{13} \\ G_{21} & G_{22} & G_{23} \\ G_{31} & G_{32} & G_{33} \\ \vdots & \vdots & \vdots \\ G_{m1} & G_{m2} & G_{m3} \end{pmatrix} = \begin{pmatrix} h_1 & k_1 & l_1 \\ h_2 & k_2 & l_2 \\ h_3 & k_3 & l_3 \\ \vdots & \vdots & \vdots \\ h_m & k_m & l_m \end{pmatrix} \begin{pmatrix} q_{x1} & q_{x2} & q_{x3} \\ q_{y1} & q_{y2} & q_{y3} \\ q_{z1} & q_{z2} & q_{z3} \end{pmatrix}, \quad (\text{S33})$$

where $m \geq 3$. If the equation is over-determined, it can be solved in the usual least-squares manner, *e.g.*,

$$[Q] = \{[H]^T [H]\}^{-1} [H]^T [G]. \quad (\text{S34})$$

The resulting q_{pn} are the coordinates of the basis vectors within the laboratory reference frame. Since the $\{335\}$ RLPs lie within the $\{110\}$ zones, we only directly derive the base diagonals of the unit cell. The [100] and [010] basis vectors are a linear combination of these: $|\vec{q}_{100}| = |\vec{q}_{010}| = |\vec{q}_{110} + \vec{q}_{\bar{1}\bar{1}0}|/2$. The analytical results are provided in Table SIII.

Recall that the RLPs are three-dimensional and the diffraction plane defined by the diffractometer's source and detector may intersect the RLPs obliquely. Any misalignment of the two low-precision axes, azimuth ϕ and tilt χ , results in missing the true center of the RLP. Additionally, the x-ray line source has significant axial divergence which extends the RLPs further outward from the diffraction plane. Since we do not calibrate the ϕ and χ axes, we block the data into two sets corresponding to $\phi \approx 0^\circ$ and $\phi \approx 90^\circ$ and analyze them separately. Henceforth we assume the two basis vectors \vec{q}_{110} and $\vec{q}_{\bar{1}\bar{1}0}$ are orthogonal.

From this analysis we find that the measured InSb lattice constant is 6.480 Å, which compares well with the expected value of 6.4793 Å (Straumanis 1965). The $\alpha\text{-SnGe}$ film's in-plane lattice constant of 6.480 Å matches the substrate's lattice constant, confirming coherency to the substrate lattice and unrelaxed, elastic strain. The lattice tilt ψ of the substrate and film with respect to the laboratory reference frame are the same and negligible. Tilt can be determined directly from the \vec{q}_{001} vectors, with $\psi=0.08^\circ$ and 0.18° for azimuths $\phi=0^\circ$ and $\phi=90^\circ$, respectively. The $\{\vec{q}_{001}\}$ and $\{\vec{q}_{110}\}$ are orthogonal with a deviation of $<0.004^\circ$ for the substrate and $<0.03^\circ$ for the film, consistent with the assumed tetragonal geometry.

The relaxed cubic lattice constant $a(x)$ of the tetragonally distorted $\text{Sn}_{1-x}\text{Ge}_x$ alloy is then calculated from the measured out-of-plane and in-plane lattice constants a_\perp and a_\parallel , respectively, using elasticity theory (Freund & Suresh 2004). The in-plane strain ϵ_\parallel and out-of-plane strain ϵ_\perp are related by Eq. (S23). Substituting the definitions of strain (S21,S22) into Eq. (S23) and solving for $a(x)$ yields

$$a(x) = \frac{a_\perp + (2C_{12}/C_{11})a_\parallel}{1 + 2C_{12}/C_{11}}. \quad (\text{S35})$$

TABLE SII. Measured peak positions of reciprocal lattice points (hkl) taken by x-ray diffraction of a $\text{Sn}_{0.945}\text{Ge}_{0.055}$ film (50 nm) on a InSb (001) substrate. ϕ = azimuthal angle; ω = incident angle; 2θ = detector angle; q_x = abscissa; q_z = ordinate; $|q_{hkl}|$ = modulus of reciprocal lattice vector; d_{hkl} = interplanar distance; and, a_{hkl} = lattice constant derived from d_{hkl} . rlu = reciprocal lattice units.

	$\phi(^{\circ})$	h	k	l	Geometry ^a	$\omega(^{\circ})$	$2\theta(^{\circ})$	$q_x(\text{rlu})$	$q_z(\text{rlu})$	$ q_{hkl} (\text{rlu})$	$d_{hkl}(\text{\AA})$	$a_{hkl}(\text{\AA})$
InSb	0.00	0	0	4	sym	28.4735	56.790	-0.00065	0.47555	0.47555	1.6198	6.4793
	0.00	3	3	5	GI	10.9655	102.411	0.50348	0.59495	0.77940	0.9883	6.4809
	0.27	$\bar{3}$	$\bar{3}$	5	GE	91.6100	102.420	-0.50507	0.59367	0.77945	0.9883	6.4805
	90.00	0	0	4	sym	28.5687	56.790	-0.00144	0.47555	0.47555	1.6198	6.4793
	90.13	3	$\bar{3}$	5	GI	91.7100	102.440	-0.50608	0.59296	0.77956	0.9881	6.4796
	90.13	$\bar{3}$	3	5	GE	11.0800	102.431	0.50247	0.59595	0.77951	0.9882	6.4800
	-0.43	3	3	5	GI	10.9355	102.431	0.50397	0.59468	0.77951	0.9882	6.4800
α -SnGe	0.00	0	0	4	sym	28.8085	57.460	-0.00066	0.48068	0.48068	1.6025	6.4100
	0.00	3	3	5	GI	11.7766	103.391	0.50368	0.60175	0.78473	0.9816	6.4369
	0.27	$\bar{3}$	$\bar{3}$	5	GE	91.7700	103.340	-0.50528	0.60004	0.78445	0.9820	6.4391
	90.00	0	0	4	sym	28.8987	57.450	-0.00146	0.48060	0.48061	1.6028	6.4111
	90.13	3	$\bar{3}$	5	GI	91.8700	103.420	-0.50619	0.59985	0.78488	0.9814	6.4356
	90.13	$\bar{3}$	3	5	GE	11.8300	103.351	0.50265	0.60233	0.78451	0.9819	6.4386
	-0.43	3	3	5	GI	11.4055	103.351	0.50396	0.60123	0.78451	0.9819	6.4386

^a Incident beam and diffracted beam configuration: sym = symmetrical; GI = grazing incidence; and, GE = grazing exit

TABLE SIII. Basis vectors derived from reciprocal lattice points (hkl) represented in the laboratory reference frame. q_{\parallel} corresponds to the appropriate in-plane direction; q_{\perp} corresponds to the out-of-plane direction; d_{hkl} is the interplanar distance in the $[hkl]$ direction.

	hkl	$q_{\parallel}(\text{rlu})$	$q_{\perp}(\text{rlu})$	$d_{hkl}(\text{\AA})$
InSb	110	0.16809	0.00021	4.5826
	001	-0.00016	0.11887	6.4803
	$\bar{1}\bar{1}0$	0.16811	0.00051	4.5822
	001	-0.00037	0.11888	6.4794
	100,010	0.11886	0.00036	6.4804
α -SnGe	110	0.16813	0.00028	4.5817
	001	-0.00016	0.12019	6.4090
	$\bar{1}\bar{1}0$	0.16811	0.00041	4.5822
	001	-0.00036	0.12021	6.4077
	100,010	0.11888	0.00035	6.4798

We assume that ratios of the elastic constants of the α - $\text{Sn}_{1-x}\text{Ge}_x$ film follows Vegard's Law, see Table SI. The ratios of $2C_{12}/C_{11}$ are 0.85 and 0.75 for α -Sn and Ge, respectively, giving a ratio of 0.84 for the assumed composition, $x=0.055$. Using this value along with a_{\perp} and a_{\parallel} derived from XRD measurements gives a lattice constant of 6.442 \AA for the α - $\text{Sn}_{0.945}\text{Ge}_{0.055}$ pseudomorphic film, consistent with the lattice constant of 6.443 \AA determined directly from Vegards rule applied to lattice constants for $x=0.055$.

In summary, the analysis of the XRD data shows that the α - $\text{Sn}_{0.945}\text{Ge}_{0.055}$ film grown on the InSb (001) substrate is highly crystalline and coherent to the substrate lattice. This epilayer ($x=0.055$) shows signs of the onset of plastic relaxation but is otherwise elastically strained.

ADDITIONAL REFERENCES

- G. Dresselhaus, A.F. Kip, and C. Kittel, Phys. Rev. **98**, 368 (1955).
- J. M. Luttinger, Phys. Rev. **102**, 1030 (1956).
- G. E. Pikus and G. L. Bir, Fiz. Tverd. Tela **1**, 1642 (1959) [Sov. Phys. Solid State **1**, 1502 (1960)].
- M. Cardona, J. Phys. Chem. Solids **24**, 1543 (1963).
- M. E. Straumanis and C. D. Kim. J. Appl. Phys. **36**, 3822 (1965)
- M. Cardona, Solid State Commun. **5**, 233 (1967).
- B. L. Booth and A. W. Ewald, Phys. Rev. **168**, 805 (1968).
- P. Lawaetz, Phys. Rev. B **4**, 3460 (1971).
- W. Leung and L. Liu, Phys. Rev. B **7**, 718 (1973).
- L. Viña, S. Logothetidis, and M. Cardona, Phys. Rev. B **30**, 1979 (1984).
- M. Cardona and N. E. Christensen, Phys. Rev. B **35**, 6182 (1987); **36**, 2906 (1987) (E).
- C. G. Van de Walle, Phys. Rev. B **39**, 1871 (1989).
- S. Logothetidis, M. Cardona, and M. Garriga, Phys. Rev. B **43**, 11950 (1991).
- T. Brudevoll, D. S. Citrin, M. Cardona, and N. E. Christensen, Phys. Rev. B **48**, 8629 (1993).
- C. Persson, A. Ferreira da Silva, R. Ahuja, and B. Johansson, J. Cryst. Growth **231**, 397 (2001).
- S. T. Pantelides and S. Zollner, *Silicon-Germanium Carbon Alloys: Growth, Properties and Applications*, (Taylor & Francis, New York, NY, 2002).
- P. F. Fewster, *X-ray scattering from Semiconductors*, 2nd ed. (Imperial College, London, 2003).
- L. B. Freund and S. Suresh, *Thin Film Materials: Stress, Defect Formation, and Surface Evolution*, (Cambridge University Press, Cambridge, 2004).

- J. Liu, D. D. Cannon, K. Wada, Y. Ishikawa, D. T. Danielson, S. Jongthammanurak, J. Michel, and L. Kimerling, *Phys. Rev. B* **70**, 155309 (2004).
- V. R. D'Costa, W. Wang, Q. Zhou, E. S. Tok, and Y. C. Yeo, *Appl. Phys. Lett.* **104**, 022111 (2014).
- A.M. Kiefer, G.J. Grzybowski, S.A. Chastang, B. B. Clafin, in *Photonics Society Summer Topical Meeting Series (SUM)*, (IEEE, Piscataway, 2017), pp 3-4.